Structural, electronic, and transport properties of quintuple atomic Janus monolayers Ga$_2$SX_2 (X = O, S, Se, Te): First-principles predictions

Nguyen N. Hieu [1,2,*] Huynh V. Phuc [3] A. I. Kartamyshev,[4,5] and Tuan V. Vu [4,5,†]

[1]*Institute of Research and Development, Duy Tan University, Da Nang 550000, Vietnam*
[2]*Faculty of Natural Sciences, Duy Tan University, Da Nang 550000, Vietnam*
[3]*Division of Theoretical Physics, Dong Thap University, Cao Lanh 870000, Vietnam*
[4]*Division of Computational Physics, Institute for Computational Science, Ton Duc Thang University, Ho Chi Minh City 700000, Vietnam*
[5]*Faculty of Electrical & Electronics Engineering, Ton Duc Thang University, Ho Chi Minh City 700000, Vietnam*

Two-dimensional Janus structures with vertical intrinsic electric fields exhibit many interesting physical properties that are not possible with symmetric materials. We systematically investigate the structural, electronic, and transport properties of quintuple-layer atomic Janus Ga$_2$SX_2 (X = O, S, Se, Te) monolayers using the first-principles calculations. The stability of the Janus structures is evaluated via the analysis of their phonon dispersion curves, cohesive and formation energies, and elastic constants. The existence of a vertical internal electric field due to the lack of mirror symmetry has resulted in a vacuum level difference between the two sides of the investigated Janus structures. At the ground state, while the Janus Ga$_2$SO$_2$ is metallic, the other three configurations (Ga$_2$S$_3$, Ga$_2$SSe$_2$, and Ga$_2$STe$_2$) are semiconductors with indirect band gaps. The electronic properties of Ga$_2$SX_2 monolayers can be altered by strain engineering. In particular, the indirect–direct band gap and semiconductor-metal phase transitions were observed when the biaxial strain was introduced. The carrier mobilities of the semiconducting Janus monolayers are directional anisotropic due to their anisotropy of the deformation potential constant. It is found that all three semiconducting Janus monolayers have high electron mobility, up to 930.34 cm^2/V s, which is suitable for applications in next-generation electronic devices.

I. INTRODUCTION

The successful exploration of graphene [1] has greatly spurred both experimental and theoretical studies of two-dimensional (2D) layered nanomaterials. As a result, a number of new 2D structures have been found, including germanene [2], silicene [3], antimonene [4], bismuthene [5], transition-metal dichalcogenides [6,7], and monochalcogenides [8–10]. With many unique physical properties, 2D layered nanomaterials have become the hottest topic of the past two decades [11], and in fact, they have been widely applied in nanoelectronic, optoelectronic, and nanoelectromechanical (NEM) devices. In addition, a new form of 2D layered nanomaterials, vertical asymmetric Janus structure, has been reported with extraordinary physical properties [12,13]. A lot of research has been devoted to the asymmetric Janus monolayers [14,15], particularly the Janus group III monochalcogenide monolayers [16–20]. With the vertical asymmetric structures, 2D Janus structures possess many novel physical properties that do not exist in 2D buckled structures with vertical mirror symmetry.

Recently, different types of 2D five-atom-thick structures based on post-transition metals and chalcogen elements, such as Ga$_2$S$_3$ and In$_2$Se$_3$, have been experimentally synthesized

using various methods [21–25]. In$_2$S$_3$ structure has been investigated for over 100 years [26]. At the bulk form, In$_2$S$_3$ can exist in two crystalline phases, namely α-In$_2$S$_3$ and β-In$_2$S$_3$ structures [27]. Recent theoretical works have focused on the electronic and piezoelectric properties of the 2D structures of these materials [28–30]. Fu *et al.* have indicated that the $\Pi_2\Lambda_3$ (Π = Ga, In; Λ = S, Se, Te) monolayers are indirect semiconductors with the energy gap decreasing with an increasing atomic size of the Λ and Π elements [28]. In particular, these $\Pi_2\Lambda_3$ monolayers have been confirmed to serve as photocatalysts in applications for water splitting. In addition, the band gaps of Ga$_2$S$_3$, Ga$_2$Se$_3$, In$_2$S$_3$, and In$_2$Se$_3$ are highly dependent on the number of layers, and they exhibit very high in-plane piezoelectric properties [30]. More importantly, strong out-of-plane second-harmonic-generation properties in Ga$_2$S$_3$, Ga$_2$Se$_3$, In$_2$S$_3$, and In$_2$Se$_3$ structures have been reported [30]. Due to its vertical asymmetric structure, the existence of out-of-plane piezoelectricity [31] and ferroelectricity [32] has also been reported in the In$_2$Se$_3$ monolayer. Further, the coexistence of ferroelectricity and ferromagnetism in In$_2$Se$_3$-doped transition-metal atoms has been observed by Zhang *et al.* [33]. Liao *et al.* have indicated that the Ga$_2$O$_3$ monolayer is also an indirect semiconductor and its band gap depends strongly on the strain engineering [34]. In particular, the indirect–direct-band-gap transition was also found in the Ga$_2$O$_3$ monolayer when the strain was introduced [34]. The Ga$_2$O$_3$ monolayer has quite high electron mobility (about 6×10^3 cm^2/V s) and it can be increased

*hieunn@duytan.edu.vn
†Corresponding author: vuvantuan@tdtu.edu.vn

over 7×10^3 cm^2/V s by biaxial strain engineering [34]. It was found that the Ga$_2$O$_3$ monolayer was predicted to have excellent dynamic and thermal stability and is expected to be experimentally synthesized. Very recently, the Ga$_2$O$_3$ monolayer was found to have a low lattice thermal conductivity and extraordinary vibrational properties [35]. With superior physical properties, the quintuple-layer atomic structures based on the group III post-transition metals and chalcogen elements are predicted to have great advantages in applications in next-generation optoelectronic and power electronic devices.

Janus structures with two different surfaces have recently emerged as very interesting objects due to their outstanding physical properties. Although many 2D post-transition-metal chalcogenide nanosheets have been successfully synthesized experimentally [9,10,21,22], there are only a few reports on experimental synthesis of 2D Janus materials [12,13]. Inspired by the unique physical properties of the existing Janus structures and the recent successful synthesis of Ga$_2$S$_3$ experimentally [21,22], we construct and systematically investigate the structural, electronic, and transport properties of the quintuple-layer atomic Janus Ga$_2$SX_2 (X = O, S, Se, Te) monolayers using the density functional theory (DFT). In this paper, we focus first on the structural properties and stability of the Janus Ga$_2$SX_2 monolayers. The stability of the Janus monolayer is examined via an analysis of its phonon spectra as well as a mechanical stability assessment based on Born's criteria for mechanical stability. The focus of this paper is on the electronic and transport properties of the Janus Ga$_2$SX_2 monolayers. In addition, the influence of biaxial strain engineering on the electronic properties as well as the extraordinary characteristics of electron states due to the vertical asymmetrical structure of Janus monolayers will also be investigated.

II. COMPUTATIONAL DETAILS

All calculations in this work are based on the DFT method using the QUANTUM ESPRESSO code [36]. The exchange-correlation interaction was treated by the generalized gradient approximation (GGA) of Perdew-Burke-Ernzerhof (PBE) [37]. We also use the DFT-D2 approach suggested by Grimme [38] to investigate the long-range weak van der Waals interactions in quintuple-layer atomic Janus Ga$_2$SX_2 (X = O, S, Se, Te) monolayers. In addition, spin-orbit coupling (SOC) was included in self-consistent calculations for electronic states of the investigated structures [39]. The projected augmented wave (PAW) was used in our calculations to investigate the interaction between nuclei and electrons. The cutoff energy for the plane-wave basis is selected to be 500 eV (37 Ry), and a cutoff of 4500 eV (331 Ry) was used for the charge density and potential. The Brillouin zone was sampled of a $(15 \times 15 \times 1)$ k-mesh based on the Monkhorst-Pack scheme. The convergence criteria for the total energy is selected to be 10^{-6} eV, and the optimized atomic structures of the Janus monolayers were achieved when the forces on all atoms were less than 0.001 eV/Å. In all calculations, a vacuum spacing of 30 Å was adopted along the z-direction to reduce the interactions between adjacent layers. Dipole correction was included to treat the errors induced by the periodic boundary conditions in the electrostatic potential calculations of the Janus
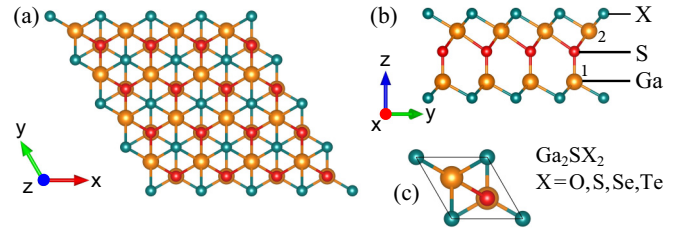

FIG. 1. The top (a) and side (b) views of Ga$_2$SX_2 (X = O, S, Se, Te). (c) Unit-cell of Ga$_2$SX_2.

structures [40]. Further, the Heyd-Scuseria-Ernzerhof functional (HSE06) [41] was also used to correct the band structure of the quintuple-layer atomic Janus Ga$_2$SX_2 monolayers.

The phonon spectra of the investigated Janus monolayers are calculated based on the density functional perturbation theory (DFPT) method [42] through the QUANTUM ESPRESSO code [36]. We built an $8 \times 8 \times 1$ supercell for calculations of phonon dispersions. A large supercell can be guaranteed to converge and yield an accurate result. The Born's criterion for mechanical stability was used to evaluate the mechanical stability of the Janus Ga$_2$SX_2 monolayers [43,44]. The mobilities of the Janus monolayers were calculated via the deformation potential approximation [45].

III. STRUCTURE AND STABILITY

The optimized atomic structures of Ga$_2$SX_2 (X = O, S, Se, Te) are shown in Fig. 1. The atomic structure of the Ga$_2$SX_2 monolayer consists of five atomic layers stacking in the order X-Ga-S-Ga-X. Note that when X = S, we get the structure Ga$_2$S$_3$. Hence, we consider four configurations, including Ga$_2$SO$_2$, Ga$_2$S$_3$, Ga$_2$SSe$_2$, and Ga$_2$STe$_2$. The unit cell of Ga$_2$SX_2 monolayers contains five atoms, and its lattice constant varies from 3.31 to 3.99 Å. The lattice constant a of Ga$_2$SX_2 increases when the element X changes from O to Te. This is because Ga-X bond lengths increase with the size of the X atoms, and the lattice constant a is proportional to Ga-X bond lengths. The calculated lattice parameters of Ga$_2$SX_2 monolayers are listed in Table I. Our calculations for the lattice parameters of Ga$_2$S$_3$ are comparable with the available data reported by Fu et al. [28]. To date, data for other monolayers of Ga$_2$SX_2 are not yet available for comparison.

To estimate the covalent bond strength in Ga$_2$SX_2 monolayers, we investigate their cohesive energy E_{coh}, which is expressed as follows:

$$E_{\text{coh}} = \frac{N_{\text{Ga}}E_{\text{Ga}} + N_{\text{S}}E_{\text{S}} + N_X E_X - E_{\text{Ga}_2\text{S}X_2}}{N_{\text{Ga}} + N_{\text{S}} + N_X}, \quad (1)$$

where E_{Ga}, E_{S}, and E_X are the single-atom energies of the Ga, S, and X elements, respectively; $E_{\text{Ga}_2\text{S}X_2}$ is the total energy of the Ga$_2$SX_2 monolayer; and N_{Ga}, N_{S}, and N_X refer to the number of atoms of Ga, S, and X in the unit cell. It is found that all four structures of Ga$_2$SX_2 are energetically favorable, and Ga$_2$SO$_2$ is the most energetically stable monolayer with $E_{\text{coh}}^{\text{Ga}_2\text{SO}_2} = 5.24$ eV. The obtained results for the cohesive energy of Ga$_2$SX_2 structures are also summarized in Table I.

TABLE I. Calculated lattice constant a, bond lengths d, bond angles θ, thickness, cohesive energy E_{coh}, and formation energy E_f of the Janus Ga_2SX_2 (X = O, S, Se, Te) monolayers (X = S refers to Ga_2S_3). Ga1 (Ga2) refers to the Ga atoms in the lower (upper) layer, as shown in Fig. 1.

	a (Å)	$d_{Ga1\text{-}S}$ (Å)	$d_{Ga2\text{-}S}$ (Å)	$d_{Ga1\text{-}X}$ (Å)	$d_{Ga2\text{-}X}$ (Å)	$\phi_{\angle Ga1XGa2}$ (deg)	$\phi_{\angle XGa1X}$ (deg)	$\phi_{\angle XGa2X}$ (deg)	Δh (Å)	E_{coh} (eV/atom)	E_f (eV/atom)
Ga_2SO_2	3.31	2.25	2.53	2.00	2.03	130.85	112.34	109.33	5.15	5.24	−0.83
Ga_2S_3	3.60	2.21	2.59	2.34	2.39	126.43	100.51	98.09	5.99	4.41	−0.74
Ga_2SSe_2	3.73	2.22	2.63	2.46	2.51	124.80	98.76	96.18	6.19	4.13	0.28
Ga_2STe_2	3.99	2.23	2.72	2.65	2.71	122.14	97.69	94.79	6.41	3.77	0.64

To consider the possibility for experimental synthesis, we also calculate the formation energy E_f of Janus Ga_2SX_2 as follows [46]:

$$E_f = \frac{E_{Ga_2SX_2} - \left(E_{Ga_2S_3} - 2E_S + 2E_X\right)}{N_{Ga} + N_S + N_X}, \quad (2)$$

where $E_{Ga_2S_3}$ is the energy of the Ga_2S_3 monolayer. By this definition, the investigated monolayers are energetically favorable when their formation energy is negative. The negative formation energy demonstrates that the realization of the Janus structure is exothermic, while the process is endothermic when E_f is positive. The formation energy of Ga_2S_3 (reference material), which is evaluated through its total energy and the chemical potential of elements in its bulk phase, is found to be −0.74 eV/at. The obtained results for the formation energy are summarized in Table I. We can see that the E_f of Janus Ga_2O_3 is the most energetically favorable structure. In a previous study, Cheng et al. revealed that the stability of 2D materials can be enhanced by biaxial tensile strain [47]. In the case of Ga_2SSe_2 and Ga_2STe_2 monolayers, our calculated results indicate that their stability is only slightly enhanced by biaxial tensile strain.

We next calculate the phonon dispersion curves of Ga_2SX_2 monolayers to evaluate their dynamical stability. The structures are confirmed to be dynamically stable when their phonon spectra contain only positive frequencies. In Fig. 2, we show the phonon spectra of Ga_2SX_2 monolayers. There are five atoms in the unit cell of Ga_2SX_2. Therefore, their phonon dispersions have 15 vibrational branches. Three acoustic branches are in the low-frequency regions, and the optical branches are in the higher-frequency regions. From Fig. 2, we can see that there is no gap between optical and acoustic phonon branches, which may lead to the strong optical-acoustic scattering. The frequencies of the optical branches decrease as the X element changes from O to Te. The crystal symmetry of Ga_2SX_2 monolayers belongs to the C_{3v} group. At the Γ-point, the vibrational modes of Ga_2SX_2 are decomposed into $\Gamma_{C_{3v}} = 5A_1 \oplus 5E$. In the optical phonon modes, both nondegenerate and doubly degenerate phonon modes occur at the high-symmetry Γ point. The nondegenerate phonon modes are the A_1 vibrational modes, and the doubly degenerate phonon modes are the E modes. The nondegenerate phonon modes (A_1) represent the out-of-plane optical (ZO) modes. Meanwhile, the doubly degenerate phonon mode at the high-symmetry Γ point is a combination of the in-plane transverse optical (TO) and the in-plane longitudinal optical (LO) modes. Sohier et al. have also proposed a method to correct the LO-TO splitting in the 2D structures based on the DFPT method [48]. More importantly, the absence of imaginary phonon modes as shown in Fig. 2 confirms that Ga_2SX_2 monolayers are dynamically stable. It is also worth noting that the obtained results for the phonon spectrum are important information for evaluating the stability of a material. Phonon calculations are necessary before synthesizing materials experimentally. However, several 2D materials are found to be both dynamically and thermodynamically stable with the theoretical calculations, but they are stable only with the supporting metal substrates [49–52].

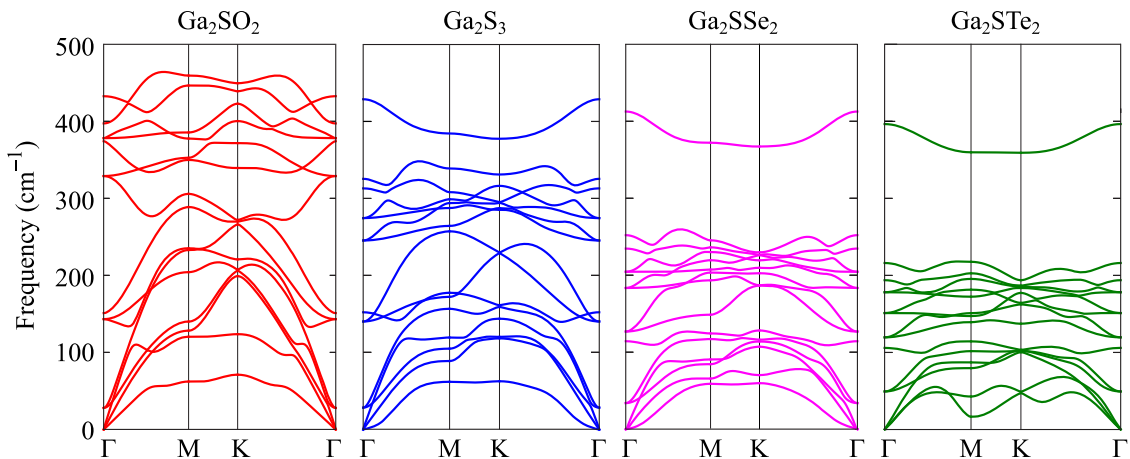Further, we examine the mechanical stability of Ga_2SX_2 monolayers based on an analysis of their elastic constants

FIG. 2. Phonon dispersion curves of Ga_2SX_2 (X = O, S, Se, Te) monolayers.

TABLE II. Calculated elastic constant C_{ij}, Young's modulus Y_{2D}, and Poisson's ratio ν of Ga_2SX_2 (X = O, S, Se, Te) monolayers.

	C_{11} (N/m)	C_{12} (N/m)	C_{66} (N/m)	Y_{2D} (N/m)	ν
Ga_2SO_2	144.59	64.21	40.19	116.08	0.44
Ga_2S_3	115.46	43.44	36.01	99.11	0.38
Ga_2SSe_2	87.33	47.17	20.08	61.68	0.54
Ga_2STe_2	77.35	27.57	24.89	67.53	0.36

C_{ij}. From the calculated elastic constants, we can evaluate the mechanical stability of the investigated materials via a comparison with Born criteria for mechanical stability. In principle, we need to calculate four independent elastic constants (C_{11}, C_{22}, C_{12}, and C_{66}). Other elastic parameters, including Young's modulus Y_{2D} and Poisson's ratio ν, can be deduced from the elastic constants C_{ij}. However, due to the symmetric structure (space group $P3m1$) of Ga_2SX_2, we have to calculate only two constants C_{11} and C_{12}. This is due to $C_{22} = C_{11}$, and C_{66} can be attained via the expression as $C_{66} = (C_{11} - C_{12})/2$. The elastic stiffness coefficients can be attained by polynomial fitting the uniaxial strain dependence of the elastic energy. The elastic energy of the investigated monolayers under uniaxial strains ε_x and ε_y along two in-plane directions is evaluated. In the present paper, the uniaxial strains ε_x and ε_y from -0.02 to 0.02 with a step of 0.005 are used to estimate the strain dependence of the elastic energy. This method has been successfully used to evaluate the elastic coefficients of 2D layered nanostructures [18,53,54].

The elastic parameters Y_{2D}, 2D shear modulus G_{2D}, and ν along the armchair/zigzag-direction for Ga_2SX_2 can be written as follows [44]:

$$Y_{2D} = \frac{C_{11}^2 - C_{12}^2}{C_{11}}, \tag{3}$$

$$G_{2D} = C_{66}, \tag{4}$$

$$\nu = \frac{C_{12}}{C_{11}}. \tag{5}$$

The calculated elastic parameters of all four configurations of Ga_2SX_2 are presented in Table II. It is demonstrated that all four structures of Ga_2SX_2 with elastic constants obey Born's criteria for mechanical stability, that is, $C_{11} > 0$ and $C_{11}^2 - C_{12}^2 > 0$ [44]. This implies that all investigated structures are mechanically stable. As shown in Table II, the value of C_{11} of Ga_2SX_2 decreases when the X element changes from O to Te. However, the value of C_{12} does not follow this trend as the value C_{12} of Ga_2SSe_2 is slightly higher than that of Ga_2S_3. This is possible because the difference in atomic size between Ga and Se is small (compared to the difference between Ga and O, S, Te) and leads to a larger coefficient of C_{12}. The Ga–Se bonds are located on the diagonal, as shown in Fig. 1. This phenomenon has also been found in the Janus GeSnSe$_2$, where the difference in atomic size between Ge and Se is also small [55]. Young's modulus of Ga_2SX_2 ranges from 20.8 to 116.08 N/m. Young's modulus of Ga_2SX_2 is generally less than that of other typical 2D layered nanomaterials, for instance, MoS$_2$ (130 N/m) [56] or graphene (340 N/m) [57]. This means that structures of Ga_2SX_2 have greater flexibility
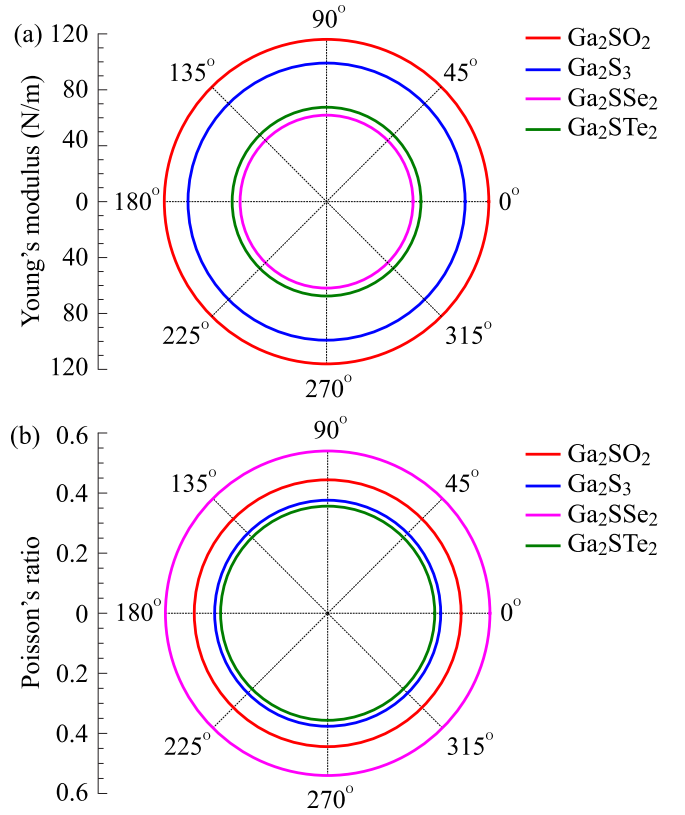

FIG. 3. Polar diagrams for (a) Young's modulus $Y_{2D}(\theta)$ and (b) Poisson's ratio $\nu(\theta)$ of Ga_2SX_2 (X = O, S, Se, Te) monolayers.

and can withstand deformations with larger amplitudes than graphene or MoS$_2$.

Depending on the in-plane symmetry, Young's modulus and Poisson's ratio of materials can be different in different directions. The angular dependence of Young's modulus $Y_{2D}(\theta)$ and Poisson's ratio $\nu(\theta)$ of the monolayers can be written as the following [58,59]:

$$Y_{2D}(\theta) = \frac{C_{11}C_{22} - C_{12}^2}{C_{11}s^4 + C_{22}c^4 - s^2c^2(2C_{12} - \Delta)}, \tag{6}$$

$$\nu(\theta) = \frac{C_{12}(s^4 + c^4) - s^2c^2(C_{11} + C_{22} - \Delta)}{C_{11}s^4 + C_{22}c^4 - s^2c^2(2C_{12} - \Delta)}, \tag{7}$$

where $\Delta = (C_{11}C_{22} - C_{12}^2)/C_{66}$, $c = \cos\theta$, and $s = \sin\theta$. Here, the angle θ defines the investigated direction with respect to the armchair one.

Polar diagrams for $Y_{2D}(\theta)$ and $\nu(\theta)$ of Ga_2SX_2 monolayers are shown in Fig. 3. It is shown that the angle-dependent Young's modulus and Poisson's ratio shapes are perfectly circular shapes, suggesting that they are independent of the angle θ, resulting from the in-plane isotropic structures of Ga_2SX_2 monolayers. This is comparable with other isotropic structures, such as graphene [60] or hexagonal Janus structures [17,61,62].

IV. ELECTRONIC PROPERTIES

In this section, we examine the electronic properties of Ga_2SX_2 monolayers via the DFT calculations. The band structures of all four Ga_2SX_2 monolayers are examined using both
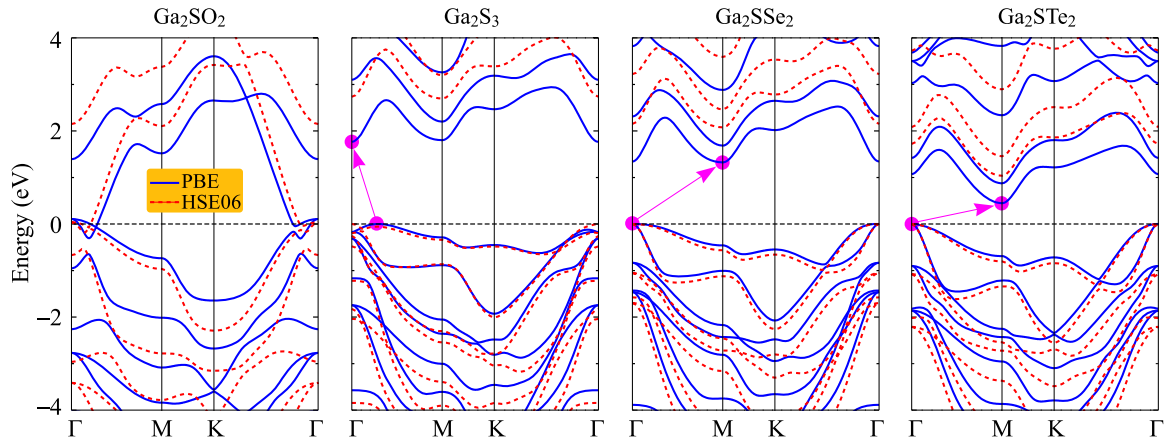
FIG. 4. Band diagrams of Ga_2SX_2 at the PBE (solid curves) and HSE06 (dashed curves) levels. Small filled circles refer to the CBM and VBM.

PBE and HSE06 methods. The band structures evaluated by the PBE and HSE06 approaches are almost the same profile as depicted in Fig. 4. All four Ga_2SX_2 monolayers are found to be nonmagnetic materials. At the ground state, the Janus Ga_2SO_2 is metallic while all other configurations (Ga_2S_3, Ga_2SSe_2, and Ga_2STe_2 monolayers) are indirect semiconductors. At the PBE, the valence-band maximum (VBM) and conduction-band minimum (CBM) of Ga_2SSe_2 and Ga_2STe_2 monolayers are located at the Γ-point and the M-point in the Brillouin zone, respectively. Meanwhile, the CBM and VBM of Ga_2S_3 are located at the Γ-point and on the ΓM path, respectively. Note that the difference in energy between the CBM and the lowest energy of the conduction band at the M-point (for Ga_2S_3) or the Γ-point (in the cases of Ga_2SSe_2 and Ga_2STe_2) is very small. Therefore, the shifting of the CBM and VBM leading to the indirect–direct-band-gap transitions can be expected when an external condition such as mechanical strain or electric field is applied. The band gaps of

Ga_2S_3, Ga_2SSe_2, and Ga_2STe_2 monolayers are calculated to be 1.77 (2.70), 1.33 (2.08), and 0.45 (1.04) eV at the PBE (HSE06), respectively. The band gap of Ga_2SX_2 decreases with the change of element X from S to Te. Our calculated result for the band gap of Ga_2S_3 is comparable with the previous DFT calculations [28]. It is noted that all four Ga_2X_3 ($X =$ O, S, Se, Te) monolayers have been previously reported to be indirect semiconductors [28,34]. However, to the best of our knowledge, there has not been any report on the Janus Ga_2SX_2 (Ga_2SO_2, Ga_2SSe_2, and Ga_2STe_2) monolayers so far.

To get insights into the atomic orbital contributions to the formation of the electronic bands, particularly the VBM and CBM, we estimate the weighted bands of all four monolayers of the Janus Ga_2SX_2 as shown in Fig. 5. In general, the orbitals of the Ga atoms have a great contribution to the conduction band, while the valence band is greatly contributed by the orbitals of the chalcogen elements. Focusing on the semiconducting monolayers, we can see that the CBM of the
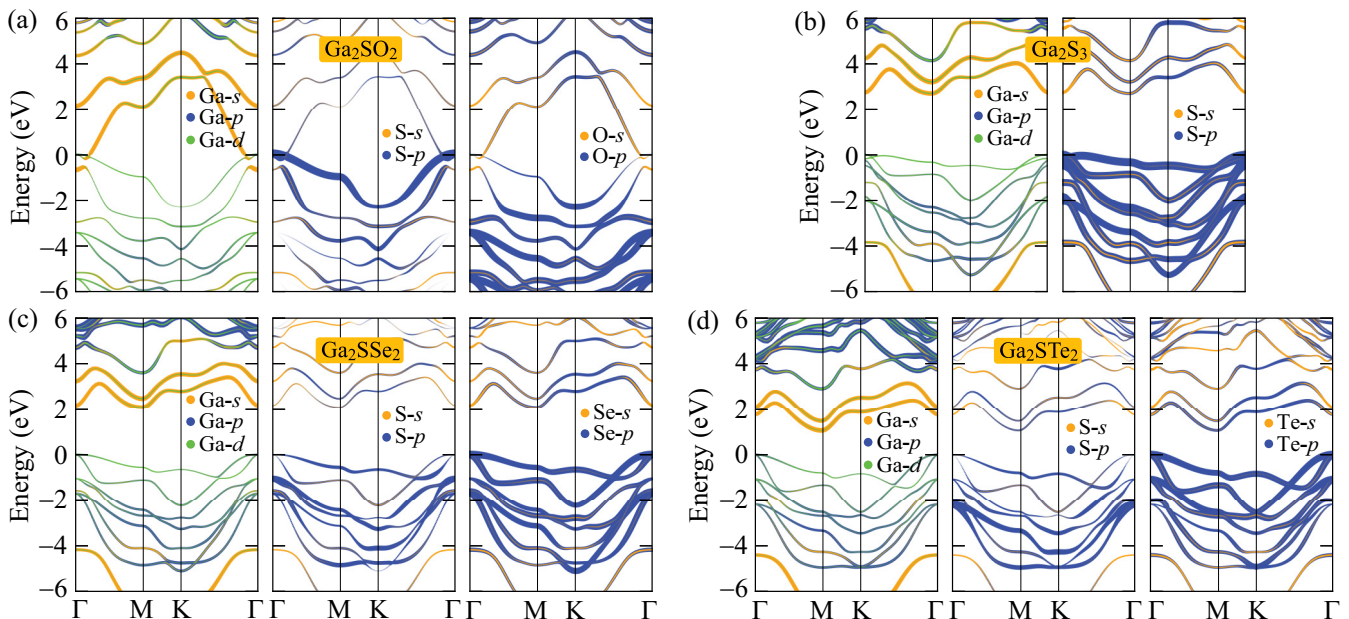

FIG. 5. Calculated weighted bands of (a) Ga_2SO_2, (b) Ga_2S_3, (c) Ga_2SSe_2, and (d) Ga_2STe_2 using the HSE06 functional.
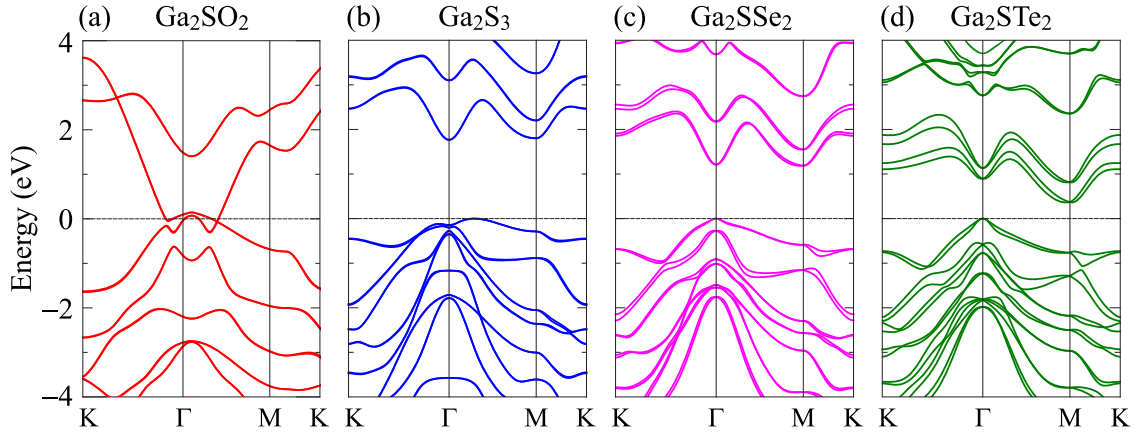
FIG. 6. Calculated band structures of Ga_2SO_2 (a), Ga_2S_3 (b), Ga_2SSe_2 (c), and Ga_2STe_2 (d) monolayers using the PBE+SOC method.

Ga_2S_3 monolayer is mainly contributed by the Ga-s orbitals, as shown in Fig. 5(b). The S-s orbitals also have a large contribution to the conduction band, although this contribution is somewhat smaller than that of the Ga-s orbitals. On the other hand, the valence band near the Fermi level, including the VBM, of the Janus Ga_2S_3 is mainly contributed by the S-p orbitals. The weighted bands of Ga_2SSe_2 and Ga_2STe_2 are almost the same as depicted in Figs. 5(c) and 5(d). In these structures, the conduction band near the Fermi level is mainly contributed by the Ga-s orbitals. In higher-energy regions (>4 eV), the contribution of the Ga-p orbitals to the conduction band is dominant. Meanwhile, the valence bands of Ga_2SSe_2 and Ga_2STe_2 are mainly contributed by the Se-p and Te-p orbitals, respectively. In addition, the contribution of the orbitals of the S atoms to the valence bands of both Ga_2SSe_2 and Ga_2STe_2 is quite small compared with that of Se and Te atoms.

The SOC effect is important in the 2D nanomaterials, particularly compounds based on heavy elements. Here, we investigate the influence of the SOC effect on the electronic properties of the Janus Ga_2SX_2 monolayers by using the PBE+SOC method. The calculated band structures along the K-Γ-M-K high-symmetry direction of the Janus Ga_2SX_2 by the PBE+SOC methods are shown in Fig. 6, from which we can see that the influence of the SOC on the band structures of Ga_2SO_2 and Ga_2S_3 is negligible. It is found that the metallic characteristics of Ga_2SO_2 are preserved, and the band gap of the Ga_2S_3 remains unchanged when the SOC is included. In addition, no band splitting was found in both Ga_2SO_2 [Fig. 6(a)] and Ga_2S_3 [Fig. 6(b)] monolayers. However, for the compounds containing heavier elements, including Ga_2SSe_2 and Ga_2STe_2 monolayers, the influence of the SOC on their electronic properties is significant. As shown in Figs. 6(c) and 6(d), we can see that, when the SOC was included, the spin degeneracy at the VBM and CBM is removed and there is small band splitting in the electronic bands of Ga_2SSe_2 and Ga_2STe_2. It is found that the band gap of Ga_2SSe_2 and Ga_2STe_2 is reduced due to the influence of the SOC effect. Due to containing the heavier element (Te), the effect of SOC on Ga_2STe_2 is greater than that of other monolayers. The calculated band gap of Ga_2STe_2 by the PBE+SOC method is found to be $E_g^{PBE+SOC} = 0.17$ eV, much smaller than that

at the PBE level (0.45 eV). The calculated band gap by the PBE+SOC method is also summarized in Table III.

One of the most important characteristics of electrons is the work function. The work function is a quantity used to evaluate the electron's ability to escape from the surfaces of a material. The work function Φ can be calculated based on the vacuum level E_{vac} and the Fermi level E_F, which can be determined from electrostatic potential calculations. The planar average electrostatic potentials of Ga_2SX_2 monolayers are shown in Fig. 7. In the vertical symmetric structures, there is only a single vacuum level. However, for asymmetric materials, there will be two different vacuum levels on the two sides of the material. The breaking of the mirror symmetry led to the formation of intrinsic electric fields inside the Janus structures [28]. Therefore, it is necessary to use dipole correction to investigate the Janus asymmetrical structures. The dipole correction is used to treat the errors induced by the periodic boundary conditions [40]. The difference in the vacuum level between two sides $\Delta\Phi$ depends on the electronegativity difference between atomic layers [63]. It is found that the vacuum level difference $\Delta\Phi$ decreases when the element X changes from O to Te, from 1.67 eV for Ga_2SO_2 to 0.94 eV for Ga_2STe_2. This changing trend is consistent with previous calculations in asymmetrical structures such as Janus group III monochalcogenide monolayers [19] and M_2Y_3 ($M =$ Al, Ga, In; $Y =$ S, Se, Te) monolayers [28]. The calculated results for $\Delta\Phi$ are listed in Table III. The difference between the vacuum levels results in two different work functions Φ_1 and Φ_2 on

TABLE III. Evaluated band gaps E_g of the Janus Ga_2SX_2 monolayers using the PBE, PBE+SOC, and HSE06 functionals, Fermi level E_F, vacuum level difference $\Delta\Phi$, and work functions Φ_1 and Φ_2. M refers to the metal.

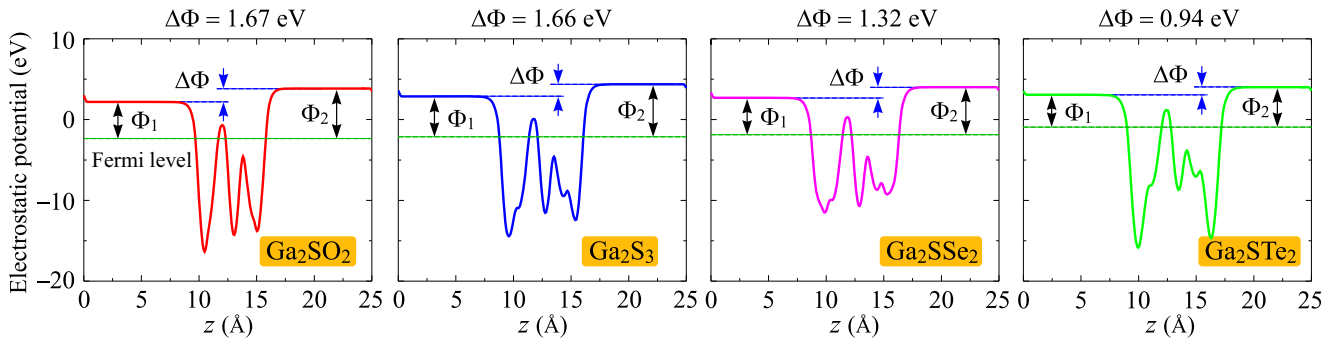|	E_g^{PBE} (eV)	$E_g^{PBE+SOC}$ (eV)	E_g^{HSE06} (eV)	E_F (eV)	$\Delta\Phi$ (eV)	Φ_1 (eV)	Φ_2 (eV)
Ga_2SO_2	M	M	M	-2.35	1.67	4.53	6.20
Ga_2S_3	1.77	1.77	2.70	-2.13	1.66	4.83	6.49
Ga_2SSe_2	1.33	1.19	2.08	-1.88	1.32	4.57	5.89
Ga_2STe_2	0.45	0.17	1.04	-0.93	0.94	4.00	4.94

FIG. 7. Planar average electrostatic potential of Ga_2SX_2 monolayers. The Fermi level is indicated by the dashed green line. $\Delta\Phi$ is the difference in the vacuum levels between two surfaces.

the two sides of Ga_2SX_2. Here Φ_1 and Φ_2 refer to the work functions on the lower side (XGa1 side in Fig. 1) and the upper side (XGa2 side), respectively. Our calculated results indicate that the work functions Φ_1 and Φ_2 of Ga_2S_3 are smaller than those of other configurations. They are $\Phi_1^{Ga_2STe_2} = 4.00$ eV and $\Phi_2^{Ga_2STe_2} = 4.94$ eV, respectively. This implies that

electrons can escape more easily from the surfaces of Ga_2STe_2 than from other configurations. The calculated results for the work function of the considered structures are also shown in Table III.

The electronic structure of 2D layered nanostructures is generally extremely sensitive to the perfection of their atomic
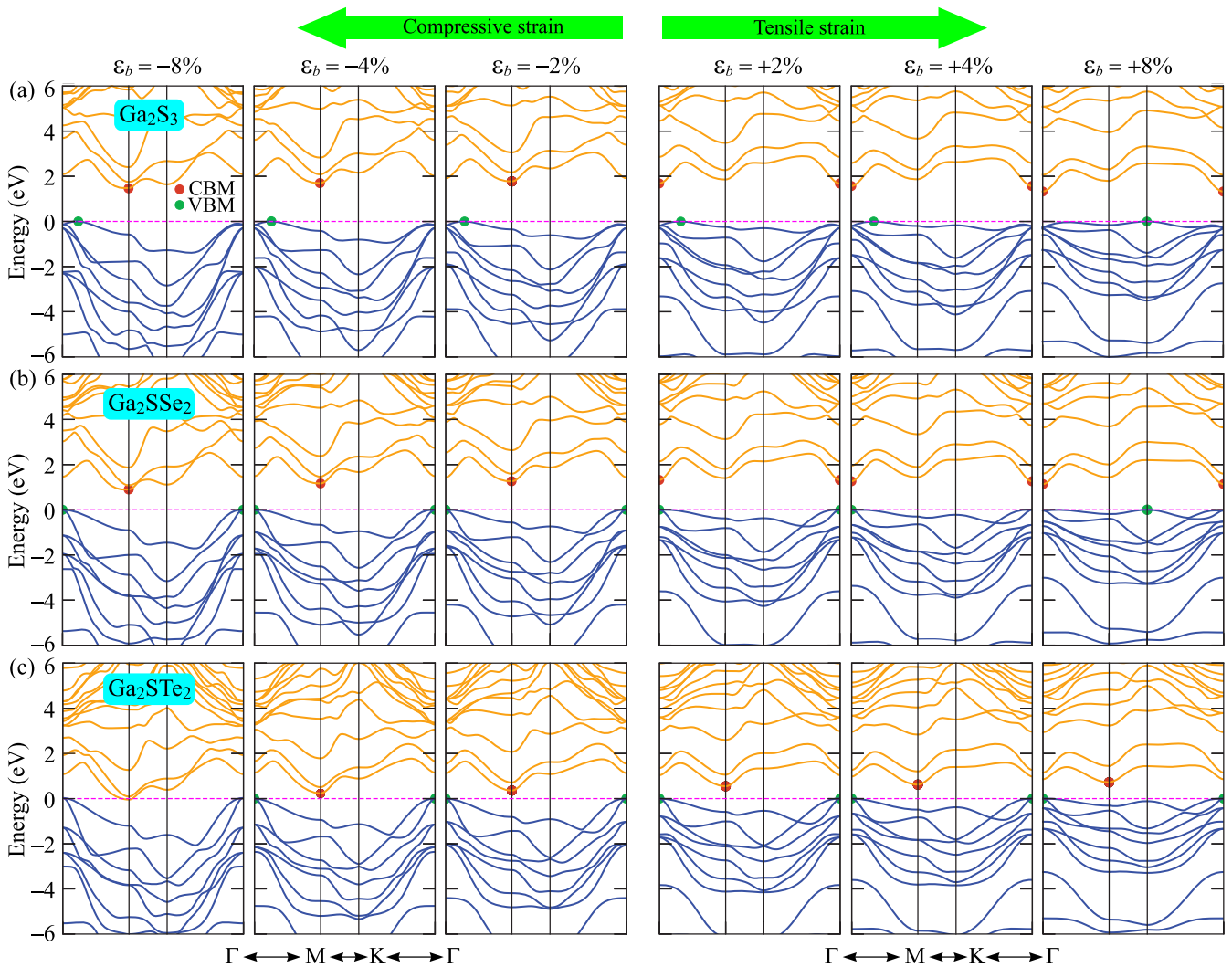

FIG. 8. Band structures of (a) Ga_2S_3, (b) Ga_2SSe_2, and (c) Ga_2STe_2 monolayers under different values of biaxial strain ε_b.
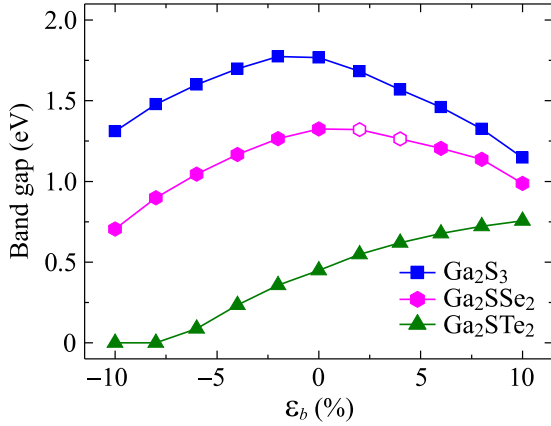
FIG. 9. Band gap of Ga_2S_3, Ga_2SSe_2, and Ga_2STe_2 monolayers as a function of the biaxial strain ε_b. Filled and open symbols refer to the indirect and direct band gaps, respectively.

structure. Strain engineering is one of the simplest and most effective ways to modulate the electron states of 2D nanostructures. Here, we study the influence of a biaxial strain on the electronic properties of three semiconducting Janus monolayers, namely Ga_2S_3, Ga_2SSe_2, and Ga_2STe_2. The biaxial strain ε_b is defined as $\varepsilon_b = (\delta - \delta_0)/\delta_0$, where δ_0 and δ stand, respectively, for the unstrained and strained lattice constants. In the present calculations, the biaxial strain ranging from -10% to 10% is applied to the three semiconducting Janus structures. The minus/plus sign indicates the compressive/tensile strain.

The band structures of Janus monolayers under the biaxial strains are shown in Fig. 8. It is revealed that the biaxial strain ε_b significantly modulated the electronic structure of the monolayers Ga_2S_3, Ga_2SSe_2, and Ga_2STe_2. When the biaxial strain is introduced, there is a shifting of the CBM in Ga_2SSe_2, and an indirect- to direct-band-gap transition was observed in Ga_2SSe_2, as shown in Fig. 8(b). Our calculations reveal that the tensile strain causes the CBM of Ga_2SSe_2 to shift from the M-point to the Γ-point, and as a result, Ga_2SSe_2 becomes a direct semiconductor at $\varepsilon_b = +2\%$. However, if the tensile strain continues to increase, its VBM tends to leave the Γ-point to reach the K-point. Obtained results show that the VBM of Ga_2SSe_2 arrived at the K-point when $\varepsilon_b = +6\%$ [not shown in Fig. 8(b)]. Consequently, Ga_2SSe_2 returns to an indirect-band-gap semiconductor with the CBM and VBM located, respectively, at the Γ- and K-point, respectively, when the tensile strain is greater than or equal to 6%. More interestingly, the strain engineering drastically changes the band gap of the monolayers, especially in the case of Ga_2STe_2 as depicted in Fig. 8(c). It is found that the band gap of Ga_2STe_2 reduces rapidly when the compressive strain is applied and the semiconductor-metal phase transition was observed at $\varepsilon_b = -8\%$ as its band gap decreases to zero. Strain-dependent band gaps of Ga_2S_3, Ga_2SSe_2, and Ga_2STe_2 monolayers are shown in Fig. 9. We can see that while the band gap of both Ga_2S_3 and Ga_2SSe_2 decreases with the tensile strain, the band gap of Ga_2STe_2 increases with tensile strain in the investigated strain range from 0 to $+10\%$. Phase transition is also a very important feature of materials. With this feature,

Ga_2SX_2 monolayers have a great potential for applications in optoelectronics and nanoelectromechanical devices.

V. TRANSPORT PROPERTIES

The applicability of materials to electronic devices depends greatly on their transport properties, especially carrier mobility. Here, we only investigate the transport characteristics of three semiconducting Janus monolayers, namely Ga_2S_3, Ga_2SSe_2, and Ga_2STe_2. The deformation potential approximation is one of the most common methods to calculate the mobility of carriers [45]. The mobility of carriers for the 2D structures can be calculated as follows [64]:

$$\mu_{2D} = \frac{e\hbar^3 C_{2D}}{k_B T m^* \overline{m} E_d^2}, \tag{8}$$

where e is the elementary charge, C_{2D} stands for the elastic modulus, E_d refers to the deformation potential constant, k_B and $\hbar$ are, respectively, the Boltzmann constant and the reduced Planck constant, m^* and $\overline{m} = \sqrt{m_x m_y}$ stand for the effective mass and the average effective mass of carriers, and $T = 300$ K is the temperature used in these calculations.

The effective mass of the carriers represents their ability to respond to the external field and directly affects their mobility. The effective masses of electron (m_e^*) and hole (m_h^*) can be obtained by fitting the parabolic function to the band edges (CBM and VBM) via the expression

$$\frac{1}{m^*} = \frac{1}{\hbar^2} \left| \frac{\partial^2 E(k)}{\partial k^2} \right|, \tag{9}$$

where $E(k)$ is the wave-vector k-dependence of energy at the CBM/VBM (in the $k_x k_y$ plane). The characteristics of the carrier transport are investigated along two different directions in the reciprocal-lattice space. From Eq. (9), we can see that the flatter the energy structure around the band edges is, the larger are the carrier effective masses. This is because the larger the radius of curvature, the smaller the second derivative $\partial^2 E(k)/\partial k^2$.

The calculated effective masses of electrons m_e^* and holes m_h^* are tabulated in Table IV. We can see that both m_e^* and m_h^* are directionally isotropic along the two transport directions. This is due to the symmetry of the band structures around the band edges of the Janus Ga_2SX_2. Our calculated results demonstrate that m_h^* is much higher than m_e^* in all three investigated monolayers. This suggests that electrons will respond to the external field faster than holes and may lead to electron mobility being higher than that of holes. This result is consistent with the band structures of the monolayers as illustrated in Fig. 4, with the band structures around the VBM being flatter than those around the CBM. Also, the electron effective mass m_e^* of Ga_2SSe_2 ($0.36m_0$) is slightly higher than that of Ga_2S_3 ($0.25m_0$) and Ga_2STe_2 ($0.24m_0$). Here, m_0 is the free-electron mass.

From Eq. (8), we can see that the mobility of carriers depends not only on the effective masses of carriers but also on the elastic modulus C_{2D} and particularly the deformation potential constant E_d. The elastic modulus C_{2D} for 2D

TABLE IV. Calculated effective mass of carriers m^*, elastic modulus C_{2D}, deformation potential constant E_d, and mobility of carriers μ along the two transport directions x and y of Ga_2S_3, Ga_2SSe_2, and Ga_2STe_2 monolayers. m_0 is the free-electron mass.

		m_x^* (m_0)	m_y^* (m_0)	C_{2D}^x (N/m)	C_{2D}^y (N/m)	E_d^x (eV)	E_d^y (eV)	μ_x (cm^2/V s)	μ_y (cm^2/V s)
Electron	Ga_2S_3	0.25	0.25	75.04	75.02	−7.36	−10.09	476.36	253.33
	Ga_2SSe_2	0.36	0.36	63.66	63.65	−8.02	−4.10	87.17	599.29
	Ga_2STe_2	0.24	0.24	51.23	51.27	−7.92	−4.38	152.15	930.34
Hole	Ga_2S_3	0.69	0.69	75.04	75.02	−5.21	−9.54	104.36	82.38
	Ga_2SSe_2	2.67	2.67	63.66	63.65	−7.78	−7.86	4.83	1.56
	Ga_2STe_2	1.32	1.32	51.23	51.27	−8.56	−8.66	9.25	7.79

materials is evaluated by the following formula:

$$C_{2D} = \frac{1}{S_0}\frac{\partial^2 E}{\partial \varepsilon_{uni}^2}, \tag{10}$$

where E is the total energy, ε_{uni} refers to the uniaxial strain along the two transport directions x and y, and S_0 is the area of the optimized unit cell. The deformation potential constant E_d can be expressed as

$$E_d = \frac{\Delta E_{edge}}{\varepsilon_{uni}}, \tag{11}$$

where ΔE_{edge} stands for the energy shifting of the band edges with respect to the vacuum level. The positions of band edges (CBM and VBM) and energy shifting are investigated within the uniaxial strain range from −1% to 1% along the two transport directions x and y. By fitting the strain-dependent energy and band energies of the VBM and CBM with respect to the vacuum energy, we can obtain the elastic modulus and deformation potential constant [64,65]. The energy shifting and the band-edge positions as a function of the uniaxial strain ε_{uni} are shown in Fig. 10. Our obtained calculations indicate that the elastic modulus C_{2D} is almost the same along the two transport

directions. The calculated results for the elastic modulus C_{2D} and the deformation potential constant E_d of the Janus Ga_2S_3, Ga_2SSe_2, and Ga_2STe_2 monolayers are listed in Table IV. We can see that the deformation potential constant E_d of Ga_2S_3, Ga_2SSe_2, and Ga_2STe_2 monolayers is quite anisotropic along the transport directions. The anisotropy of the deformation potential constant has also been reported recently in similar structures, such as Ga_2Te_3, Al_2Se_3, or Al_2Te_3 monolayers [28]. For example, the ratio of $|E_d^x/E_d^y|$ for electrons in the Ga_2Te_3 monolayer is up to 3.87 [28]. This will lead to the carrier mobility anisotropy along the transport directions.

Based on the calculated results for m^*, C_{2D}, and E_d, we can estimate the carrier mobilities along the two transport directions μ_x and μ_y as listed in Table IV. It is found that the carrier mobilities are not only anisotropic between electrons and holes, but they are also anisotropic in the two transport directions x and y. The electron mobility along the y-direction μ_y^e of Ga_2STe_2 is the highest, up to 930.34 cm^2/V s. The μ_x^e of Ga_2STe_2 is lower than its electron mobility along the y direction, $\mu_x^e(Ga_2STe_2) = 152.15$ cm^2/V s. This demonstrates the anisotropy of the electron mobility along the two transport directions. Such anisotropy of carrier mobility has also been
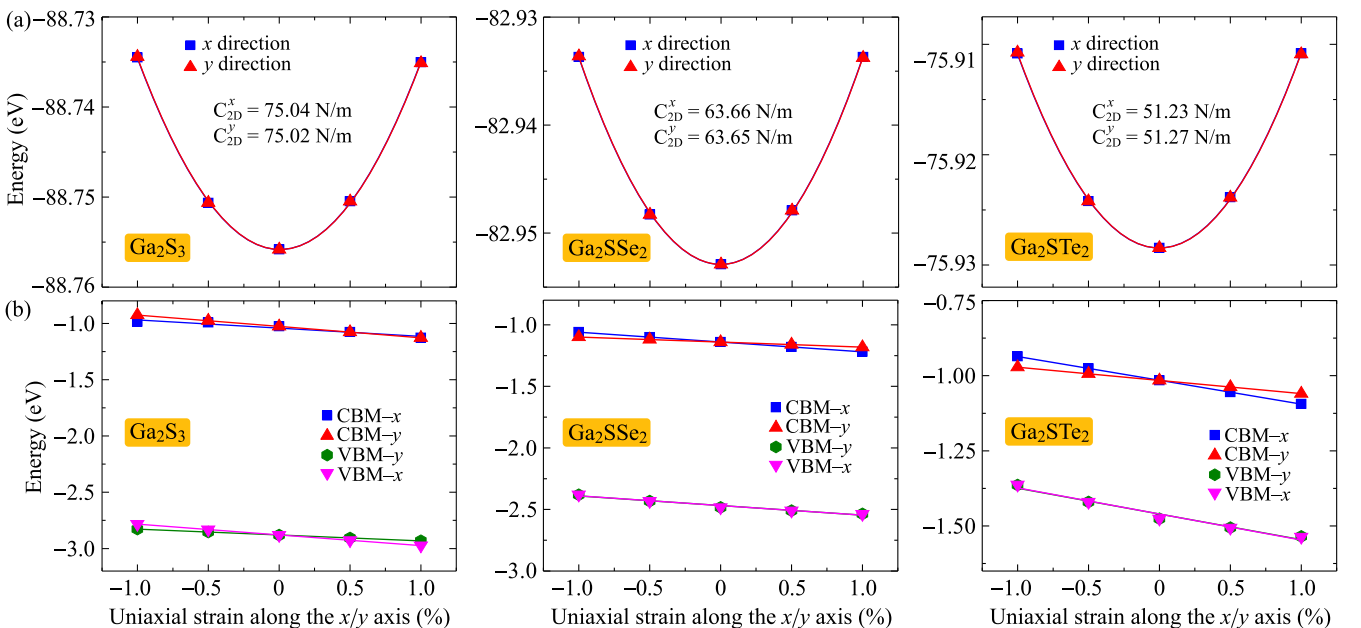

FIG. 10. (a) The energy shifting and (b) band-edge positions as a function of the uniaxial strain along two transport directions of Ga_2S_3, Ga_2SSe_2, and Ga_2STe_2 monolayers. The solid lines indicate the fitting curves.

reported previously in similar materials, such as In_2STe_2 with $\mu_y^e/\mu_x^e = 1.44$ [66] or Al_2Te_3 with $\mu_x^e/\mu_y^e = 7.16$ [28]. The obtained results also indicate that there is a huge disparity of mobility between holes and electrons. The hole mobility is much smaller than the electron mobility because the effective mass of the hole is much heavier than the effective mass of the electron and will reduce the hole mobility as mentioned above. From Table IV, we can see that the investigated monolayers have high electron mobility [μ_y^e of all three investigated Janus monolayers is higher than the electron mobility of the transition metal dichalcogenide monolayer MoS_2 (200 cm^2/V s) [67]], suggesting that they may be potential nanomaterials for applications in nanoelectronics.

VI. CONCLUSION

In summary, we have considered the structural, stability, electronic, and transport properties of the Janus Ga_2SX_2 ($X =$ O, S Se, Te) monolayers by employing first-principles based on DFT calculations. At the ground state, while the Janus Ga_2S_3, Ga_2SSe_2, and Ga_2STe_2 are indirect semiconductors, the Janus Ga_2SO_2 exhibits metallic characteristics with both the conduction and valence band crossing the Fermi level. Interestingly, when the biaxial strain was introduced, the semiconductor-metal phase transition is found in the Janus Ga_2STe_2 monolayer, and the indirect–direct–indirect-band-gap transitions are observed in the Janus Ga_2SSe_2 monolayer. The electron mobilities of the semiconducting Janus monolayers are high directional anisotropic due to the anisotropy of their deformation potential constant. Also, the mobility of holes is much smaller than that of electrons. Since the electronic properties can be easily controlled by strain, and especially with high electron mobility, the Janus Ga_2SX_2 monolayers have great potential for applications in nanoelectronics and nanoelectromechanical devices. Our results not only give a deeper understanding of the physical properties of novel quintuple-layer atomic Janus Ga_2SX_2 monolayers, but they also guide further studies in both theory and experiment.

[1] K. S. Novoselov, A. K. Geim, S. V. Morozov, D. Jiang, Y. Zhang, S. V. Dubonos, I. V. Grigorieva, and A. A. Firsov, Science **306**, 666 (2004).

[2] M. Derivaz, D. Dentel, R. Stephan, M.-C. Hanf, A. Mehdaoui, P. Sonnet, and C. Pirri, Nano Lett. **15**, 2510 (2015).

[3] S. Cahangirov, M. Topsakal, E. Aktürk, H. Şahin, and S. Ciraci, Phys. Rev. Lett. **102**, 236804 (2009).

[4] M. Fortin-Deschênes, O. Waller, T. O. Menteş, A. Locatelli, S. Mukherjee, F. Genuzio, P. L. Levesque, A. Hébert, R. Martel, and O. Moutanabbir, Nano Lett. **17**, 4970 (2017).

[5] F. Yang, A. O. Elnabawy, R. Schimmenti, P. Song, J. Wang, Z. Peng, S. Yao, R. Deng, S. Song, Y. Lin, M. Mavrikakis, and W. Xu, Nat. Commun. **11**, 1088 (2020).

[6] D. Kong, H. Wang, J. J. Cha, M. Pasta, K. J. Koski, J. Yao, and Y. Cui, Nano Lett. **13**, 1341 (2013).

[7] G. Deokar, D. Vignaud, R. Arenal, P. Louette, and J.-F. Colomer, Nanotechnology **27**, 075604 (2016).

[8] D. D. Vaughn, R. J. Patel, M. A. Hickner, and R. E. Schaak, J. Am. Chem. Soc. **132**, 15170 (2010).

[9] P. Hu, Z. Wen, L. Wang, P. Tan, and K. Xiao, ACS Nano **6**, 5988 (2012).

[10] S. Acharya, M. Dutta, S. Sarkar, D. Basak, S. Chakraborty, and N. Pradhan, Chem. Mater. **24**, 1779 (2012).

[11] N. A. Poklonski, S. A. Vyrko, A. I. Siahlo, O. N. Poklonskaya, S. V. Ratkevich, N. N. Hieu, and A. A. Kocherzhenko, Mater. Res. Express **6**, 042002 (2019).

[12] A.-Y. Lu, H. Zhu, J. Xiao, C.-P. Chuu, Y. Han, M.-H. Chiu, C.-C. Cheng, C.-W. Yang, K.-H. Wei, Y. Yang, Y. Wang, D. Sokaras, D. Nordlund, P. Yang, D. A. Muller, M.-Y. Chou, X. Zhang, and L.-J. Li, Nat. Nanotechnol. **12**, 744 (2017).

[13] J. Zhang, S. Jia, I. Kholmanov, L. Dong, D. Er, W. Chen, H. Guo, Z. Jin, V. B. Shenoy, L. Shi, and J. Lou, ACS Nano **11**, 8192 (2017).

[14] Q.-F. Yao, J. Cai, W.-Y. Tong, S.-J. Gong, J.-Q. Wang, X. Wan, C.-G. Duan, and J. H. Chu, Phys. Rev. B **95**, 165401 (2017).

[15] M. J. Varjovi, M. Yagmurcukardes, F. M. Peeters, and E. Durgun, Phys. Rev. B **103**, 195438 (2021).

[16] T. V. Vu, C. V. Nguyen, H. V. Phuc, A. A. Lavrentyev, O. Y. Khyzhun, N. V. Hieu, M. M. Obeid, D. P. Rai, H. D. Tong, and N. N. Hieu, Phys. Rev. B **103**, 085422 (2021).

[17] T. V. Vu, V. T. T. Vi, H. V. Phuc, A. I. Kartamyshev, and N. N. Hieu, Phys. Rev. B **104**, 115410 (2021).

[18] Y. Guo, S. Zhou, Y. Bai, and J. Zhao, Appl. Phys. Lett. **110**, 163102 (2017).

[19] A. Huang, W. Shi, and Z. Wang, J. Phys. Chem. C **123**, 11388 (2019).

[20] M. Demirtas, B. Ozdemir, Y. Mogulkoc, and E. Durgun, Phys. Rev. B **101**, 075423 (2020).

[21] Y. Zheng, X. Tang, W. Wang, L. Jin, and G. Li, Adv. Funct. Mater. **31**, 2008307 (2021).

[22] H. F. Liu, K. K. A. Antwi, N. L. Yakovlev, H. R. Tan, L. T. Ong, S. J. Chua, and D. Z. Chi, ACS Appl. Mater. Interfaces **6**, 3501 (2014).

[23] J. Zhou, Q. Zeng, D. Lv, L. Sun, L. Niu, W. Fu, F. Liu, Z. Shen, C. Jin, and Z. Liu, Nano Lett. **15**, 6400 (2015).

[24] G. Almeida, S. Dogan, G. Bertoni, C. Giannini, R. Gaspari, S. Perissinotto, R. Krahne, S. Ghosh, and L. Manna, J. Am. Chem. Soc. **139**, 3005 (2017).

[25] C.-H. Ho and H.-H. Chen, Sci. Rep. **4**, 6143 (2014).

[26] A. Thiel and H. Koelsch, Z. Anorg. Chem. **66**, 288 (1910).

[27] K. Osamura, Y. Murakami, and Y. Tomiie, J. Phys. Soc. Jpn. **21**, 1848 (1966).

[28] C.-F. Fu, J. Sun, Q. Luo, X. Li, W. Hu, and J. Yang, Nano Lett. **18**, 6312 (2018).

[29] W. Ding, J. Zhu, Z. Wang, Y. Gao, D. Xiao, Y. Gu, Z. Zhang, and W. Zhu, Nat. Commun. **8**, 14956 (2017).

[30] L. Hu and X. Huang, RSC Adv. **7**, 55034 (2017).

[31] F. Xue, J. Zhang, W. Hu, W.-T. Hsu, A. Han, S.-F. Leung, J.-K. Huang, Y. Wan, S. Liu, J. Zhang, J.-H. He, W.-H. Chang, Z. L. Wang, X. Zhang, and L.-J. Li, ACS Nano **12**, 4976 (2018).

[32] C. Cui, W.-J. Hu, X. Yan, C. Addiego, W. Gao, Y. Wang, Z. Wang, L. Li, Y. Cheng, P. Li, X. Zhang, H. N. Alshareef, T. Wu, W. Zhu, X. Pan, and L.-J. Li, Nano Lett. **18**, 1253 (2018).

[33] C. Zhang, L. Zhang, C. Tang, S. Sanvito, B. Zhou, Z. Jiang, and A. Du, Phys. Rev. B **102**, 134416 (2020).

[34] Y. Liao, Z. Zhang, Z. Gao, Q. Qian, and M. Hua, ACS Appl. Mater. Interfaces **12**, 30659 (2020).

[35] G. Liu, Z. Zhang, H. Wang, G.-L. Li, J.-S. Wang, and Z. Gao, J. Appl. Phys. **130**, 105106 (2021).

[36] P. Giannozzi, S. Baroni, N. Bonini, M. Calandra, R. Car, C. Cavazzoni, D. Ceresoli, G. L. Chiarotti, M. Cococcioni, I. Dabo, A. D. Corso, S. de Gironcoli, S. Fabris, G. Fratesi, R. Gebauer, U. Gerstmann, C. Gougoussis, A. Kokalj, M. Lazzeri, L. Martin-Samos, N. Marzari, F. Mauri, R. Mazzarello, S. Paolini, A. Pasquarello, L. Paulatto, C. Sbraccia, S. Scandolo, G. Sclauzero, A. P. Seitsonen, A. Smogunov, P. Umari, and R. M. Wentzcovitch, J. Phys.: Condens. Matter **21**, 395502 (2009).

[37] J. P. Perdew, K. Burke, and M. Ernzerhof, Phys. Rev. Lett. **77**, 3865 (1996).

[38] S. Grimme, J. Comput. Chem. **27**, 1787 (2006).

[39] A. H. MacDonald, W. E. Picket, and D. D. Koelling, J. Phys. C **13**, 2675 (1980).

[40] L. Bengtsson, Phys. Rev. B **59**, 12301 (1999).

[41] J. Heyd, G. E. Scuseria, and M. Ernzerhof, J. Chem. Phys. **118**, 8207 (2003).

[42] T. Sohier, M. Calandra, and F. Mauri, Phys. Rev. B **96**, 075448 (2017).

[43] M. Born and K. Huang, Am. J. Phys. **23**, 474 (1955).

[44] R. C. Andrew, R. E. Mapasha, A. M. Ukpong, and N. Chetty, Phys. Rev. B **85**, 125428 (2012).

[45] J. Bardeen and W. Shockley, Phys. Rev. **80**, 72 (1950).

[46] W. Chen, X. Hou, X. Shi, and H. Pan, ACS Appl. Mater. Interfaces **10**, 35289 (2018).

[47] Y. C. Cheng, Z. Y. Zhu, M. Tahir, and U. Schwingenschlögl, Europhys. Lett. **102**, 57001 (2013).

[48] T. Sohier, M. Gibertini, M. Calandra, F. Mauri, and N. Marzari, Nano Lett. **17**, 3758 (2017).

[49] S.-G. Xu, X.-T. Li, Y.-J. Zhao, J.-H. Liao, W.-P. Xu, X.-B. Yang, and H. Xu, J. Am. Chem. Soc. **139**, 17233 (2017).

[50] X. Wu, J. Dai, Y. Zhao, Z. Zhuo, J. Yang, and X. C. Zeng, ACS Nano **6**, 7443 (2012).

[51] A. J. Mannix, X.-F. Zhou, B. Kiraly, J. D. Wood, D. Alducin, B. D. Myers, X. Liu, B. L. Fisher, U. Santiago, J. R. Guest, M. J. Yacaman, A. Ponce, A. R. Oganov, M. C. Hersam, and N. P. Guisinger, Science **350**, 1513 (2015).

[52] V. Kochat, A. Samanta, Y. Zhang, S. Bhowmick, P. Manimunda, S. A. S. Asif, A. S. Stender, R. Vajtai, A. K. Singh, C. S. Tiwary, and P. M. Ajayan, Sci. Adv. **4**, e1701373 (2018).

[53] K.-A. N. Duerloo, M. T. Ong, and E. J. Reed, J. Phys. Chem. Lett. **3**, 2871 (2012).

[54] W.-Z. Xiao, G. Xiao, and L.-L. Wang, J. Chem. Phys. **145**, 174702 (2016).

[55] L. Seixas, J. Appl. Phys. **128**, 045115 (2020).

[56] R. C. Cooper, C. Lee, C. A. Marianetti, X. Wei, J. Hone, and J. W. Kysar, Phys. Rev. B **87**, 035423 (2013).

[57] D. G. Papageorgiou, I. A. Kinloch, and R. J. Young, Prog. Mater. Sci. **90**, 75 (2017).

[58] N. T. Hung, A. R. T. Nugraha, and R. Saito, J. Phys. D **51**, 075306 (2018).

[59] P. Xiang, S. Sharma, Z. M. Wang, J. Wu, and U. Schwingenschlögl, ACS Appl. Mater. Interfaces **12**, 30731 (2020).

[60] E. Cadelano, P. L. Palla, S. Giordano, and L. Colombo, Phys. Rev. B **82**, 235414 (2010).

[61] S.-D. Guo, X.-S. Guo, R.-Y. Han, and Y. Deng, Phys. Chem. Chem. Phys. **21**, 24620 (2019).

[62] T.-N. Do, N. N. Hieu, N. A. Poklonski, N. T. T. Binh, C. Q. Nguyen, and N. D. Hien, RSC Adv. **11**, 28381 (2021).

[63] W. Zhou, J. Chen, Z. Yang, J. Liu, and F. Ouyang, Phys. Rev. B **99**, 075160 (2019).

[64] W. Wan, S. Zhao, Y. Ge, and Y. Liu, J. Phys.: Condens. Matter **31**, 435501 (2019).

[65] S.-D. Guo, W.-Q. Mu, Y.-T. Zhu, R.-Y. Han, and W.-C. Ren, J. Mater. Chem. C **9**, 2464 (2021).

[66] P. Wang, H. Liu, Y. Zong, H. Wen, J.-B. Xia, and H.-B. Wu, ACS Appl. Mater. Interfaces **13**, 34178 (2021).

[67] B. Radisavljevic, A. Radenovic, J. Brivio, V. Giacometti, and A. Kis, Nat. Nanotechnol. **6**, 147 (2011).